

1D Kohn anomaly in 3D topological Dirac semimetals

Shengying Yue,^{1,†} Bowen Deng,^{1,†} Yamming Liu,^{1,2,†} Yujie Quan,¹ Runqing Yang,¹ and Bolin Liao^{1,*}

¹*Department of Mechanical Engineering, University of California, Santa Barbara, CA 93106, USA*

²*School of Aerospace Engineering, Tsinghua University, Beijing, 100084, China*

Kohn anomalies are distortions of phonon dispersions in metals and semimetals caused by electron-phonon interactions. Typically, lower-dimensional materials show stronger Kohn anomalies determined by the geometry of their Fermi surfaces. For this reason, the archetypal model systems for studying Kohn anomalies have been 1D and 2D conductors. In this work, combining *ab initio* simulations and theoretical analysis, we investigate strong Kohn anomalies in 3D topological Dirac semimetals. Owing to their unique electronic structure consisting of 3D Dirac cones, we show that their Kohn anomalies have the same features as those in a 1D simple metal. By analyzing model systems ZrTe_5 and Na_3Bi , in addition to our previous results on Cd_3As_2 , we further illustrate the relationship between their strong Kohn anomalies and ultralow lattice thermal conductivities. Our work opens up a material platform to probe and understand Kohn anomalies and indicates the potential application of 3D topological Dirac semimetals as thermoelectric materials.

INTRODUCTION

Kohn anomalies, first recognized by W. Kohn in 1959[1], refer to the distortions observed in phonon dispersions in metals and semimetals caused by the resonance between the Fermi surface and certain phonon modes. Specifically, when two electronic states on the Fermi surface are parallelly connected by a phonon momentum \mathbf{q} , Kohn showed that the polarizability $\Pi(\omega, \mathbf{q})$, which describes the collective response of the conduction electrons to an external disturbance with frequency ω and wavevector \mathbf{q} , becomes non-analytic. Since phononic vibrations are screened by the conduction electrons, the non-analyticity of the polarizability at certain phonon momentum \mathbf{q} leads to abrupt changes of the phonon dispersion.

In simple metals with parabolic bands, the exact condition for Kohn anomalies to occur is $\mathbf{q} = 2\mathbf{k}_F$, where \mathbf{k}_F is the Fermi wavevector. As illustrated in Fig. 1(a)-(c), the Fermi surfaces of simple metals have different shapes in different dimensions. In a 1D conductor, the Fermi surface is simply two points separated by a distance of $2\mathbf{k}_F$, and strong Kohn anomalies at $\mathbf{q} = 2\mathbf{k}_F$ lead to the Peierls instability. In 2D and 3D simple metals, the Fermi surfaces are circles and spheres, respectively, and the Kohn anomalies happen when \mathbf{q} matches the diameter of the circle/sphere. The strength of the Kohn anomalies can be gauged by the sharp change of the static polarizability $\Pi_0(\mathbf{q})$ around $\mathbf{q} = 2\mathbf{k}_F$. The static polarizabilities can be calculated within the random phase approximation (RPA)[2] and are plotted in Fig. 1(e). It is clearly seen that Kohn anomalies are more prominent in 1D and 2D conductors in a similar manner as the van Hove singularities in the electronic density of states. For this reason, intensive research of Kohn anomalies has focused on lower

dimensional and layered conductors, such as graphite[3], layered compounds NbSe_2 [4] and TaS_2 [5], graphene[6–8], carbon nanotubes[9], other 1D conductors[10] and surface states of topological insulators[11].

Beyond simple metals with parabolic bands, emerging materials with special electronic structures can lead to distinct behaviors of Kohn anomalies. One such class of materials is the 3D topological Dirac semimetal (TDS). 3D TDS possesses linear electronic bands near the Fermi level located at discrete Dirac nodes, and therefore can be treated as 3D analogs of graphene[12, 13]. TDS has aroused extensive research interests because of their interesting electronic transport and optical properties, e.g. the Dirac fermions with ultrahigh mobilities[14–18], the unique Fermi arc surface states[19, 20] and highly temperature-sensitive optical properties[21]. Although novel electronic properties are well studied in TDS, the phonon properties and electron-phonon interactions in TDS have been less investigated so far. In a recent study[22], we reported the existence of ultrasoft optical phonons in the TDS Cd_3As_2 , which gives rise to strong phonon-phonon scatterings and a low lattice thermal conductivity. The phonon softening was attributed to potentially strong Kohn anomalies associated with the Dirac nodes. In parallel, Nguyen et al. reported the experimental observation of Kohn anomalies in a Weyl semimetal tantalum phosphide (TaP)[23], where chirality selection rules of electron-phonon scatterings limited the magnitude of the Kohn anomalies.

In this work, via first-principles calculations, we generalize the previous findings to other known members of the TDS class: zirconium pentatelluride (ZrTe_5)[24] and trisodium bismuthide (Na_3Bi)[12, 25]. We identify the existence of strong Kohn anomalies in both materials, which explains their anomalously low lattice thermal conductivities ($\sim 0.1 \text{ W/mK}$ for Na_3Bi and $\sim 0.5 \text{ W/mK}$ for ZrTe_5 at 300 K, in good agreement with a recent experiment[26]). The calculated lattice thermal conductivity of Na_3Bi at room temperature (0.094 W/mK) is

[†] These authors contributed equally to this work
^{*} bliao@ucsb.edu

the record-low value for a crystalline material, to the best of our knowledge. We further point out that the unique geometry of the Fermi surfaces of 3D TDS (two discrete points in the momentum space, as shown in Fig. 1(d)) makes their Kohn anomalies resemble those in 1D simple metals, as illustrated in Fig. 1(e). This feature presents 3D TDS as a three-dimensional material platform that displays strong Kohn anomalies in their phonon dispersions (Fig. 1(f)) and signals their potential use as thermoelectric materials.

COMPUTATIONAL DETAILS

For ZrTe_5 , the base-centered orthorhombic $Cmcm$ (D_{2h}^{17}) structure was discovered to be the most stable phase at ambient condition based on previous studies[27]. In this structure, ZrTe_3 chains run along the a axis, which are connected by zigzag Te atoms to form 2D sheets. These 2D sheets are further stacked along the b axis. The crystal structure and the conventional cell is shown in Fig. 2(a), with the corresponding Brillouin zone (BZ) shown in Fig. 2(b). For Na_3Bi , the $P\bar{3}c1$ (D_{3d}^4 , anti- LaF_3 -type)[28] and the $P6_3/mmc$ (D_{6h}^4 , Na_3As -type)[29] phases have very similar energies and there exists controversy on which phase is the true ground state. Our calculation agrees with [28] that $P\bar{3}c1$ is dynamically stable without imaginary phonon frequencies, whereas $P6_3/mmc$ is not. This is also consistent with recent optical measurements[30]. Both phases have very similar electronic structures. We analyze the $P\bar{3}c1$ phase in this work, which is shown in Fig. 2(c), where Na and Bi atoms form distorted honeycomb layers. The corresponding Brillouin zone is shown in Fig. 2(d). We highlight the 3D Dirac cones' positions and the high-symmetry points in the BZs of the two TDSs. We also present the anisotropic Dirac cones of Na_3Bi [12] in Fig. 2(d).

All of the structural optimizations, electronic properties and phonon behaviors were calculated based on the density functional theory (DFT) by employing the Vienna *ab initio* simulation package (VASP)[31, 32]. The projector augmented wave (PAW) method[33, 34] and generalized gradient approximation (GGA) with the Perdew-Burke-Ernzerhof (PBE) exchange-correlation functional were adopted[35]. For ZrTe_5 , the van der Waals (vdW) corrected optB86b-vdw functional[36, 37] was used throughout all calculations because ZrTe_5 is a layered material for which the vdW correction is essential to obtain the correct inter-layer distance[38, 39]. The plane wave cutoff energy was set to 350 eV for both TDSs[28, 39]. The Monkhorst-Pack k meshes $9 \times 9 \times 4$ were taken for ZrTe_5 , and $8 \times 8 \times 8$ for Na_3Bi . The k -mesh density and the energy cutoff of augmented plane waves were checked to ensure the convergence. Full optimizations were applied to both structures with the Hellmann-Feynman forces tolerance 0.0001eV/Å. The

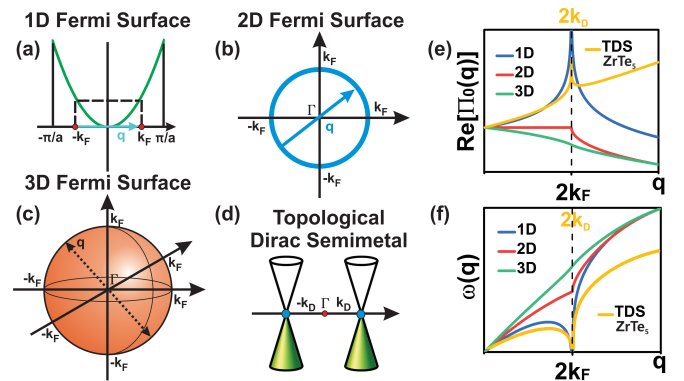


FIG. 1. (a-d) Schematics of the Fermi surfaces of simple metals in different dimensions and the topological Dirac semimetals (TDSs). (e) A comparison of the real parts of the static polarizability $\Pi_0(\mathbf{q})$ of the simple metals in different dimensions and the TDSs, e.g. ZrTe_5 , showing the strong Kohn anomaly in TDSs with similar features as that in 1D simple metals. (f) Schematic illustrating the distortion of phonon dispersions due to Kohn anomalies in different systems.

spin-orbit coupling (SOC) effect was included through all calculations[28].

To evaluate the phonon dispersions and lattice thermal conductivities of ZrTe_5 and Na_3Bi , we further calculated the second and third order inter-atomic force constants (IFCs) using the finite-displacement approach[40]. Our adoption of the finite-displacement approach implicitly determines that only the static, or adiabatic, Kohn anomalies can be captured[3], while the dynamic effect[23] requires explicit electron-phonon coupling calculations[6] beyond the scope of the current work. In the calculations of the second and third order IFCs, we adopted $3 \times 3 \times 1$ supercells (108 atoms)[39] for ZrTe_5 and $2 \times 2 \times 2$ supercells (192 atoms)[28] for Na_3Bi . The phonon dispersions based on the second order IFCs were calculated using the PHONOPY package[40]. The interactions between atoms were taken into account up to sixth nearest neighbors in third-order IFC calculations. We calculated the lattice thermal conductivities by solving the phonon Boltzmann transport equation (BTE) iteratively as implemented in ShengBTE[41, 42]. The q -mesh sampling for the BTE calculations of ZrTe_5 and Na_3Bi was $8 \times 8 \times 20$ and $12 \times 12 \times 12$, respectively. The convergence of the lattice thermal conductivities with respect to the q -mesh density and the interaction distance cutoff was checked.

RESULTS AND DISCUSSIONS

Our calculated electronic band structures of ZrTe_5 and Na_3Bi are shown in Fig. 3(a, c), which are consistent with previous reports[27, 28]. In ZrTe_5 , 3D Dirac nodes are located half-way along the $\Gamma - \text{Y}$ direction, which

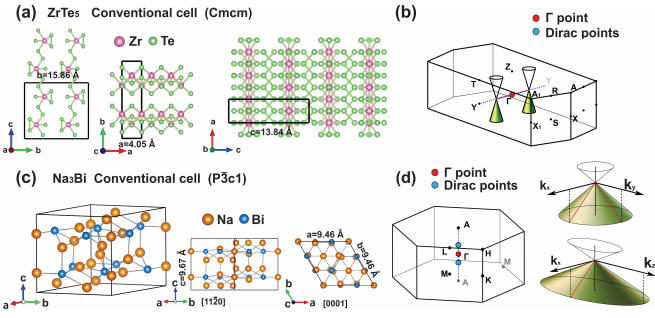


FIG. 2. (a) The crystal structure of ZrTe_5 with calculated lattice constants. (b) The first Brillouin zone of ZrTe_5 , where the Γ point and the locations of the two Dirac points are marked. (c) The crystal structure of Na_3Bi with calculated lattice constants. (d) The first Brillouin zone of Na_3Bi , where the Γ point and the locations of the two Dirac points are marked. The inset shows the anisotropic shape of the 3D Dirac cones in Na_3Bi .

aligns with the layer-stacking b -axis in the conventional cell. In Na_3Bi , the 3D Dirac nodes are located along the $\Gamma - \text{A}$ direction, which is also the stacking axis of the honeycomb layers. Fig. 3(b, d) highlight the Dirac nodes of ZrTe_5 and Na_3Bi . One key difference between ZrTe_5 and Na_3Bi is that the Dirac nodes are isotropic in ZrTe_5 , but highly anisotropic in ZrTe_5 . In ZrTe_5 , the Fermi velocity (v_F) at the Dirac nodes is approximately 3.32×10^5 m/s and independent of the direction, which is close to the previous experimental result measured by angle-resolved photoemission spectroscopy (ARPES) [43]. In contrast, in Na_3Bi , v_F is highly anisotropic [28] ($v_F^- \approx 5.10 \times 10^5$ m/s and $v_F^+ \approx 0.318 \times 10^5$ m/s, as labeled in Fig. 3(d)). The low Fermi velocity between the two Dirac nodes in Na_3Bi indicates that the electronic band is nearly flat in this region. Therefore, its Fermi surface is closer to a circular “disk”, as compared to the two well-separated Dirac nodes in ZrTe_5 . This distinct feature leads to different behaviors of Kohn anomalies in these two TDSs, which will be discussed later.

The Fermi surface being two discrete nodes gives rise to two possible types of Kohn anomalies associated with intra-node or inter-node electron-phonon scatterings, which were similarly observed in graphene [3, 6]. In the intra-node case, one electron within the vicinity of one Dirac node is scattered to another electronic state near the same node, mediated by a phonon with a wavevector $\mathbf{q} \approx \mathbf{0}$. These processes are responsible for phonon anomalies near the Brillouin zone center. In the inter-node case, one electron close to one Dirac node is scattered to another electronic state near the other node, mediated by a phonon with a wavevector matching the distance between the two nodes, $\mathbf{q} \approx 2\mathbf{k}_D$, where \mathbf{k}_D marks the location of one Dirac node, as illustrated in Fig. 3(b,d). Thus in general, Kohn anomalies in TDSs are expected to cause distortions of phonon dispersions

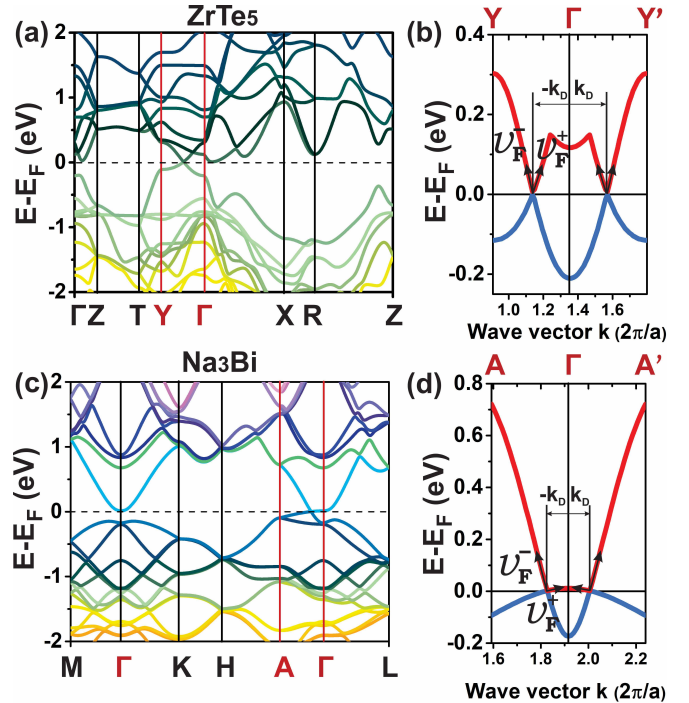


FIG. 3. (a, c) The calculated electronic band structures of ZrTe_5 and Na_3Bi along high-symmetry lines, showing the Dirac nodes along the $\Gamma - \text{Y}$ direction in ZrTe_5 and the $\Gamma - \text{A}$ direction in Na_3Bi . (b, d) Highlights of the electronic band structures near the Dirac nodes in ZrTe_5 and Na_3Bi , with the Fermi velocities near the Dirac nodes labeled. For ZrTe_5 , the Fermi velocity at the Dirac node is isotropic ($v_F^- = v_F^+ \approx 3.32 \times 10^5$ m/s), whereas for Na_3Bi the Fermi velocity at the Dirac node is anisotropic ($v_F^- \approx 5.10 \times 10^5$ m/s and $v_F^+ \approx 0.318 \times 10^5$ m/s).

near $\mathbf{q} \approx \mathbf{0}$ and $\mathbf{q} \approx 2\mathbf{k}_D$.

The direct cause of Kohn anomalies are the singularities in the electronic polarizability $\Pi(\omega, \mathbf{q})$. $\Pi(\omega, \mathbf{q})$ associated with the two Dirac nodes D1 and D2 can be calculated in the linear response regime within the random phase approximation as [44]:

$$\Pi(i\omega, \mathbf{q}) = -\frac{1}{\beta} \sum_n \int \frac{d^3\mathbf{k}}{(2\pi)^3} \text{Tr}[G_2(i\omega + i\omega_n, \mathbf{q} + \mathbf{k}_2) G_1(i\omega_n, \mathbf{k}_1)], \quad (1)$$

where $\beta = k_B T$, $G_i(i\omega_n, \mathbf{k}_i) = \frac{1}{i\omega_n - \mathcal{H}(\mathbf{k}_i)}$ is the Dirac fermion propagator of electrons near the i th Dirac node, \mathbf{k}_i is the wavevector of the electrons involved. For isotropic Dirac nodes, such as those in ZrTe_5 , the Dirac fermion Hamiltonian of one Dirac node can be written as [30, 45]

$$\mathcal{H}(\mathbf{k}) = v_F \mathbf{k} \cdot \boldsymbol{\sigma}, \quad (2)$$

where $\boldsymbol{\sigma}$ are the Pauli matrices. In this case, Eq. 1 can be evaluated analytically, as done by Nguyen et al. [23]

in the case of a Weyl semimetal. We independently verified their results in the case of Dirac semimetals, where the only difference is that the chiral selections rules of electron-phonon scatterings are lifted. The main conclusion is that, near $\mathbf{q} \approx \mathbf{0}$ and $\mathbf{q} \approx 2\mathbf{k}_D$, the real part of $\Pi(\omega, \mathbf{q})$ diverges as

$$\text{Re}[\Pi(\omega, \mathbf{q})] \sim \ln |v_F q' - \omega|, \quad (3)$$

where $\mathbf{q}' = \mathbf{q}$ for the intra-node case and $\mathbf{q}' = \mathbf{q} - 2\mathbf{k}_D$ for the inter-node case. Therefore, the electronic polarizability diverges logarithmically when $\omega = v_F q'$. Phonons very close to $\mathbf{q} = \mathbf{0}$ and $\mathbf{q} = 2\mathbf{k}_D$ satisfy this condition since v_F is much higher than the speed of sound in these materials.

We plot the real part of the static dielectric function $\epsilon_0(\mathbf{q}) = 1 + \frac{4\pi\Pi_0(\mathbf{q})}{q^2}$ of ZrTe_5 with realistic parameters extracted from our first-principles calculations in Fig. 4(a), showing the diverging peaks when $\mathbf{q} = \mathbf{0}$ and $\mathbf{q} = 2\mathbf{k}_D$, corresponding to intra-node and inter-node electron-phonon transitions, respectively. Importantly, the logarithmic divergence behavior of the electronic po-

larizability in 3D TDSs is the same as that in a 1D simple metal[2], where it is known that Kohn anomalies are strong and can even lead to structural instabilities (Peierls transitions). The calculated phonon dispersion of ZrTe_5 is shown in Fig. 4(b). Since the Dirac nodes are located half-way between Γ and Y , it is expected that Kohn anomalies should occur near Γ (intra-node scatterings) and Y (inter-node scatterings). Indeed, we observed a soft optical phonon mode at Γ with a slight kink near the zone center and a strong dip of the acoustic modes near Y , as marked down by arrows in the figure. The same features were also observed in previous studies of ZrTe_5 [26]. The observation of static Kohn anomalies in ZrTe_5 is also consistent with our previous report of another TDS Cd_3As_2 [22]. These phonon features are expected to significantly enlarge the available phase space for phonon scatterings and reduce the lattice thermal conductivity, which we will analyze quantitatively in a later section.

The case of Na_3Bi is more complicated as the Dirac cones are highly anisotropic[46]. The effective Hamiltonian for electrons near the anisotropic Dirac cones can be written as[46]:

$$\mathcal{H}(\mathbf{k}) = v_0 k_z I_4 + \begin{pmatrix} -v_D k_z & v_\perp(k_x + ik_x) & 0 & 0 \\ v_\perp(k_x - ik_x) & v_D k_z & 0 & 0 \\ 0 & 0 & -v_D k_z & -v_\perp(k_x - ik_x) \\ 0 & 0 & -v_\perp(k_x + ik_x) & v_D k_z \end{pmatrix} \quad (4)$$

where I_4 is a 4×4 identity matrix, k_z is the electronic wavevector along the $\Gamma - A$ direction originating from the Dirac nodes, k_x and k_y are wavevectors along two orthogonal directions that are perpendicular to k_z as shown in Fig. 2(d), $v_0 \pm v_D = v_F^\mp$ are the two Fermi velocities as labeled in Fig. 3(d), and v_\perp is the Fermi velocity along directions that are perpendicular to k_z . The polarizability in this case can be calculated by plugging the Hamiltonian in Eq. 4 into Eq. 1. Due to the complexity of this Hamiltonian, we found no analytical results and instead integrated Eq. 1 numerically, with realistic parameters extracted from our first-principles simulation. The resulted static dielectric function is plotted in Fig. 4(c). Interestingly, in this case the singularity only appears near the Brillouin zone center ($\mathbf{q} \approx \mathbf{0}$). Physically, this is due to the very flat electronic band between the Dirac nodes that leads to a disk-like Fermi surface, so that a “patch” of phonons near the Brillouin zone center satisfy the selection rules of electron-phonon scatterings that contribute to the Kohn anomaly. This finding is confirmed in our first-principles calculation of the phonon dispersions of Na_3Bi , which is shown in Fig. 4(d). A very soft optical phonon mode appears at the zone center with a frequency below 0.5 THz and a “kink” in

the dispersion at Γ point that is reminiscent of Kohn anomalies in graphite and graphene[3]. This feature will similarly significantly enlarge the phonon-phonon scattering phase space and lead to a reduced lattice thermal conductivity, as understood in certain bulk thermoelectric materials[47] and two-dimensional materials[48]. We quantitatively analyze the impact of the Kohn anomalies on the lattice thermal conductivity of ZrTe_5 and Na_3Bi next.

In Fig. 5(a) and (c), we show the calculated lattice thermal conductivity of ZrTe_5 and Na_3Bi as a function of the temperature. Both materials show very low and anisotropic thermal conductivities. In the case of ZrTe_5 , the lattice thermal conductivities along three axes are all different, with the one along the layer-stacking direction (b-axis) being the lowest. Our results agree with the previous calculation and experiment by Zhu et al.[26]. More interestingly, we observed anomalous peaks in the phonon-phonon scattering rates of the low-frequency acoustic modes in ZrTe_5 , as shown in Fig. 5(b): one near 0.3 THz and the other near 0.7 THz, corresponding to the Kohn anomalies at Y and Γ , respectively. Due to the sparsity of the scattering data in this low frequency range and the computational challenge to

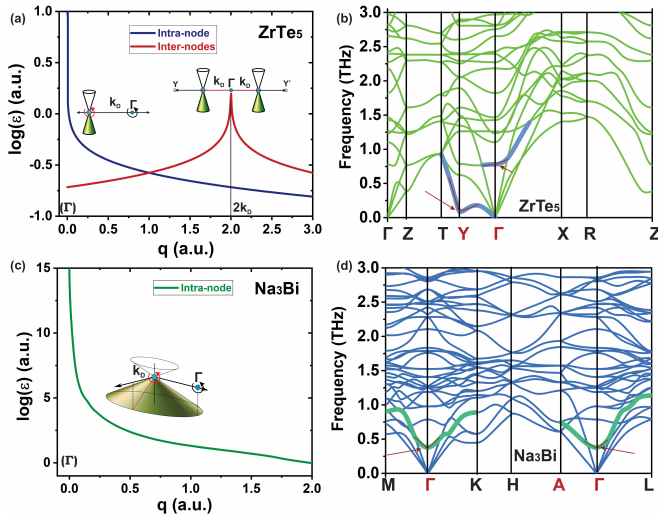


FIG. 4. (a,c) The calculated real parts of the static dielectric functions of ZrTe₅ and Na₃Bi, respectively, showing the singularities at $\mathbf{q} = \mathbf{0}$ and $\mathbf{q} = 2\mathbf{k}_D$ corresponding to intra-node and inter-node scatterings. (b,d) The calculated phonon dispersions of the two TDSs. The phonon softenings induced by Kohn anomalies are highlighted.

increase the sampling density further, the peak around 0.3 THz is not conclusive, but the peak around 0.7 THz is quite prominent, providing strong evidence that the Kohn anomalies associated with the Dirac nodes in ZrTe₅ significantly contribute to its low lattice thermal conductivity. In the case of Na₃Bi, the thermal conductivity within the honeycomb layer is isotropic, which is different from the cross-plane value. Both thermal conductivities are extremely low: around 0.1 W/mK at room temperature. These values, if confirmed experimentally, will be among the lowest for crystalline materials. We analyzed the phonon-phonon scattering rates, which are shown in Fig. 5(b), and found a significant enhancement of phonon scatterings around 0.4 THz, which coincides with the frequency of the soft optical phonon mode at the zone center due to the Kohn anomaly. The existence of such soft optical phonon modes signals that Na₃Bi is close to a structural instability, similar to Cd₃As₂. Our result suggests that this incipient structural instability has the same origin as the 1D Peierls transition due to 1D-like strong Kohn anomalies associated with the Dirac nodes and might be a universal feature of topological semimetals. The extremely low lattice thermal conductivity of Na₃Bi implies its potential application as a thermoelectric material, but its known sensitivity to air exposure might hinder practical uses.

CONCLUSION

In summary, we identified the existence of strong Kohn anomalies in two representative TDSs, ZrTe₅ and Na₃Bi,

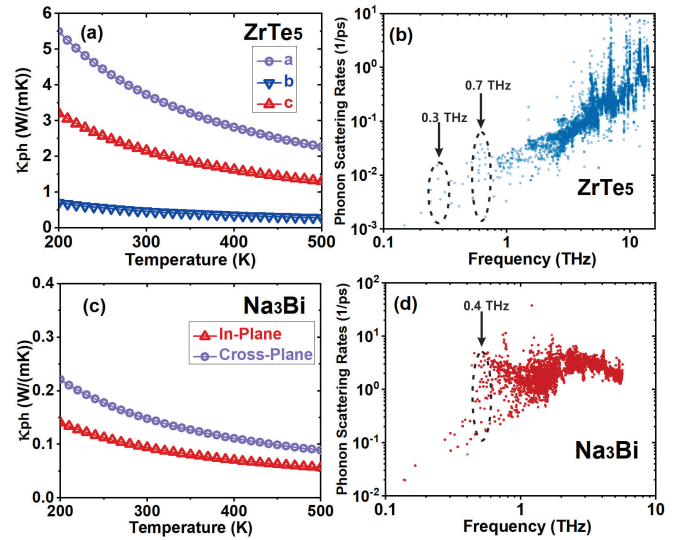


FIG. 5. (a,c) The calculated lattice thermal conductivities of ZrTe₅ and Na₃Bi, respectively, as a function of temperature. (b,d) The calculated phonon-phonon scattering rates in ZrTe₅ and Na₃Bi as a function of the phonon frequency.

through first-principles simulation and theoretical analysis of the electronic polarizability. We further quantified the contribution of the strong Kohn anomalies to the low lattice thermal conductivities. In particular, we pointed out that the 3D Dirac nodes give rise to strong Kohn anomalies similar to those in 1D metals, which suggests that the TDSs are close to a Peierls-like structural instability. Our study alludes to deep connections between the electronic structure and lattice dynamics and exemplifies the rich phonon physics in topological materials.

ACKNOWLEDGMENTS

We acknowledge helpful discussions with Mingda Li and Xi Dai. This work is based on research supported by the U.S. Department of Energy, Office of Basic Energy Sciences, Division of Materials Science and Engineering through the Early Career Research Program under the award number DE-SC0019244. Y.L. acknowledges the support from the Tsinghua Scholarship for Undergraduate Overseas Studies.

- [1] W. Kohn, Phys. Rev. Lett. **2**, 393 (1959).
- [2] X. Zhu, Y. Cao, J. Zhang, E. Plummer, and J. Guo, Proceedings of the National Academy of Sciences **112**, 2367 (2015).
- [3] S. Piscanec, M. Lazzari, F. Mauri, A. Ferrari, and J. Robertson, Physical Review Letters **93**, 185503 (2004).
- [4] N. Wakabayashi, H. Smith, and R. Shanks, Physics Letters A **50**, 367 (1974).

[5] P. Williams, G. Parry, and C. Scrub, *Philosophical Magazine* **29**, 695 (1974).

[6] M. Lazzari and F. Mauri, *Physical Review Letters* **97**, 266407 (2006).

[7] D. L. Mafra, L. M. Malard, S. K. Doorn, H. Htoon, J. Nilsson, A. H. Castro Neto, and M. A. Pimenta, *Phys. Rev. B* **80**, 241414 (2009).

[8] W.-K. Tse, B. Y.-K. Hu, and S. Das Sarma, *Phys. Rev. Lett.* **101**, 066401 (2008).

[9] S. Piscanec, M. Lazzari, J. Robertson, A. C. Ferrari, and F. Mauri, *Phys. Rev. B* **75**, 035427 (2007).

[10] B. Renker, H. Rietschel, L. Pintschovius, W. Gläser, P. Brüesch, D. Kuse, and M. Rice, *Physical Review Letters* **30**, 1144 (1973).

[11] X. Zhu, L. Santos, C. Howard, R. Sankar, F. C. Chou, C. Chamon, and M. El-Batanouny, *Phys. Rev. Lett.* **108**, 185501 (2012).

[12] Z. K. Liu, B. Zhou, Y. Zhang, Z. J. Wang, H. M. Weng, D. Prabhakaran, S.-K. Mo, Z. X. Shen, Z. Fang, X. Dai, Z. Hussain, and Y. L. Chen, *Science* **343**, 864 (2014).

[13] S. M. Young, S. Zaheer, J. C. Y. Teo, C. L. Kane, E. J. Mele, and A. M. Rappe, *Phys. Rev. Lett.* **108**, 140405 (2012).

[14] Z. Wang, H. Weng, Q. Wu, X. Dai, and Z. Fang, *Phys. Rev. B* **88**, 125427 (2013).

[15] Y. Ominato and M. Koshino, *Phys. Rev. B* **89**, 054202 (2014).

[16] M. Orlita, D. Basko, M. Zholudev, F. Teppe, W. Knap, V. Gavrilenco, N. Mikhailov, S. Dvoretskii, P. Neugebauer, C. Faugeras, *et al.*, *Nature Physics* **10**, 233 (2014).

[17] M. Neupane, S.-Y. Xu, R. Sankar, N. Alidoust, G. Bian, C. Liu, I. Belopolski, T.-R. Chang, H.-T. Jeng, H. Lin, *et al.*, *Nature Communications* **5**, 3786 (2014).

[18] T. Schumann, M. Goyal, H. Kim, and S. Stemmer, *APL Materials* **4**, 126110 (2016).

[19] X. Wan, A. M. Turner, A. Vishwanath, and S. Y. Savrasov, *Phys. Rev. B* **83**, 205101 (2011).

[20] S.-Y. Xu, C. Liu, S. K. Kushwaha, R. Sankar, J. W. Krizan, I. Belopolski, M. Neupane, G. Bian, N. Alidoust, T.-R. Chang, H.-T. Jeng, C.-Y. Huang, W.-F. Tsai, H. Lin, P. P. Shibayev, F.-C. Chou, R. J. Cava, and M. Z. Hasan, *Science* **347**, 294 (2015).

[21] H. T. Chorsi, S. Yue, P. P. Iyer, M. Goyal, T. Schumann, S. Stemmer, B. Liao, and J. A. Schuller, *arXiv preprint arXiv:1907.12105* (2019).

[22] S. Yue, H. T. Chorsi, M. Goyal, T. Schumann, R. Yang, T. Xu, B. Deng, S. Stemmer, J. A. Schuller, and B. Liao, *Physical Review Research* **1**, 033101 (2019).

[23] T. Nguyen, F. Han, N. Andrejevic, R. Pablo-Pedro, A. Apte, Y. Tsurimaki, Z. Ding, K. Zhang, A. Alatas, E. E. Alp, *et al.*, *arXiv preprint arXiv:1906.00539* (2019).

[24] H. Weng, X. Dai, and Z. Fang, *Phys. Rev. X* **4**, 011002 (2014).

[25] J. Xiong, S. K. Kushwaha, T. Liang, J. W. Krizan, M. Hirschberger, W. Wang, R. J. Cava, and N. P. Ong, *Science* **350**, 413 (2015).

[26] J. Zhu, T. Feng, S. Mills, P. Wang, X. Wu, L. Zhang, S. T. Pantelides, X. Du, and X. Wang, *ACS Applied Materials & Interfaces* **10**, 40740 (2018).

[27] Y. Zhou, J. Wu, W. Ning, N. Li, Y. Du, X. Chen, R. Zhang, Z. Chi, X. Wang, X. Zhu, *et al.*, *Proceedings of the National Academy of Sciences* **113**, 2904 (2016).

[28] X. Cheng, R. Li, Y. Sun, X.-Q. Chen, D. Li, and Y. Li, *Phys. Rev. B* **89**, 245201 (2014).

[29] Z. Wang, Y. Sun, X.-Q. Chen, C. Franchini, G. Xu, H. Weng, X. Dai, and Z. Fang, *Physical Review B* **85**, 195320 (2012).

[30] G. S. Jenkins, C. Lane, B. Barbiellini, A. B. Sushkov, R. L. Carey, F. Liu, J. W. Krizan, S. K. Kushwaha, Q. Gibson, T.-R. Chang, H.-T. Jeng, H. Lin, R. J. Cava, A. Bansil, and H. D. Drew, *Phys. Rev. B* **94**, 085121 (2016).

[31] G. Kresse and J. Furthmüller, *Phys. Rev. B* **54**, 11169 (1996).

[32] G. Kresse and J. Furthmüller, *Computational Materials Science* **6**, 15 (1996).

[33] P. E. Blöchl, *Phys. Rev. B* **50**, 17953 (1994).

[34] G. Kresse and D. Joubert, *Phys. Rev. B* **59**, 1758 (1999).

[35] J. P. Perdew, K. Burke, and M. Ernzerhof, *Phys. Rev. Lett.* **77**, 3865 (1996).

[36] J. Klimeš, D. R. Bowler, and A. Michaelides, *Journal of Physics: Condensed Matter* **22**, 022201 (2009).

[37] J. c. v. Klimeš, D. R. Bowler, and A. Michaelides, *Phys. Rev. B* **83**, 195131 (2011).

[38] Z. Fan, Q.-F. Liang, Y. Chen, S.-H. Yao, and J. Zhou, *Scientific Reports* **7**, 45667 (2017).

[39] C. Wang, H. Wang, Y. Chen, S.-H. Yao, and J. Zhou, *Journal of Applied Physics* **123**, 175104 (2018).

[40] A. Togo, F. Oba, and I. Tanaka, *Phys. Rev. B* **78**, 134106 (2008).

[41] W. Li, J. Carrete, N. A. Katcho, and N. Mingo, *Computer Physics Communications* **185**, 1747 (2014).

[42] W. Li, N. Mingo, L. Lindsay, D. A. Broido, D. A. Stewart, and N. A. Katcho, *Phys. Rev. B* **85**, 195436 (2012).

[43] Y. Zhang, C. Wang, L. Yu, G. Liu, A. Liang, J. Huang, S. Nie, X. Sun, Y. Zhang, B. Shen, *et al.*, *Nature Communications* **8**, 15512 (2017).

[44] A. A. Abrikosov, L. P. Gorkov, and I. E. Dzyaloshinski, *Methods of Quantum Field Theory in Statistical Physics* (Courier Corporation, 2012).

[45] A. Burkov, *Nature Materials* **15**, 1145 (2016).

[46] G. Jenkins, C. Lane, B. Barbiellini, A. Sushkov, R. Carey, F. Liu, J. Krizan, S. Kushwaha, Q. Gibson, T.-R. Chang, *et al.*, *Physical Review B* **94**, 085121 (2016).

[47] S. Lee, K. Esfarjani, T. Luo, J. Zhou, Z. Tian, and G. Chen, *Nature Communications* **5**, 3525 (2014).

[48] S.-Y. Yue, T. Xu, and B. Liao, *Materials Today Physics* **7**, 89 (2018).